VEGF$_{121}$-Conjugated Mesoporous Silica Nanoparticle: A Tumor Targeted Drug Delivery System

Shreya Goel,[†,⊗] Feng Chen,[‡,⊗] Hao Hong,[‡] Hector F. Valdovinos,[§] Reinier Hernandez,[§] Sixiang Shi,[†] Todd E. Barnhart,[§] and Weibo Cai*[,†,‡,§,∥,⊥]

[†]Materials Science Program, University of Wisconsin−Madison, Madison, Wisconsin 53705, United States
[‡]Department of Radiology, University of Wisconsin−Madison, Madison, Wisconsin 53705, United States
[§]Department of Medical Physics, University of Wisconsin−Madison, Madison, Wisconsin 53705, United States
[∥]University of Wisconsin Carbone Cancer Center, Madison, Wisconsin 53705, United States

S Supporting Information

ABSTRACT: The vascular endothelial growth factor (VEGF)/VEGF receptor (VEGFR) signaling cascade plays a critical role in tumor angiogenesis and metastasis and has been correlated with several poorly prognostic cancers such as malignant gliomas. Although a number of anti-VEGFR therapies have been conceived, inefficient drug administration still limits their therapeutic efficacy and raises concerns of potential side effects. In the present work, we propose the use of uniform mesoporous silica nanoparticles (MSNs) for VEGFR targeted positron emission tomography imaging and delivery of the anti-VEGFR drug (i.e., sunitinib) in human glioblastoma (U87MG) bearing murine models. MSNs were synthesized, characterized and modified with polyethylene glycol, anti-VEGFR ligand VEGF$_{121}$ and radioisotope ^{64}Cu, followed by extensive in vitro, in vivo and ex vivo studies. Our results demonstrated that a significantly higher amount of sunitinib could be delivered to the U87MG

tumor by targeting VEGFR when compared with the non-targeted counterparts. The as-developed VEGF$_{121}$-conjugated MSN could become another attractive nanoplatform for the design of future theranostic nanomedicine.

KEYWORDS: VEGFR, mesoporous silica nanoparticle, drug delivery, vasculature targeting, positron emission tomography
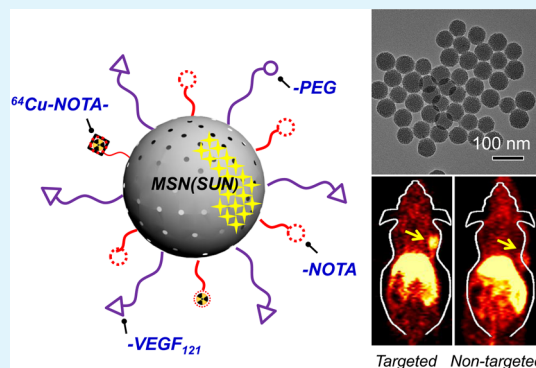
■ INTRODUCTION

Angiogenesis (i.e., the formation of new blood vessels) is a key hallmark of cancer growth and metastasis.[1,2] Noninvasive imaging of angiogenesis can allow for much earlier cancer diagnosis and better prognosis, ultimately paving the way for personalized molecular medicine.[3] It is well-known that, for a tumor to grow beyond ∼2 mm³, it must develop a network of blood vessels to supply nutrients and oxygen and to remove waste products.[4] A number of growth factor receptor pathways form the molecular basis of angiogenesis, of which the vascular endothelial growth factor (VEGF) family of proteins and receptors is an integral member.[5] Research also showed that activation of the VEGF pathway could trigger a signaling cascade that promotes endothelial cell growth and migration from pre-existing vasculature.[6] Due to its well-established role in angiogenesis, radiolabeled ligands, such as VEGF$_{121}$, bevacizumab, etc., which target the VEGF receptor (i.e., VEGFR), have successfully been developed for early and sensitive lesion detection by using positron emission tomography (PET) and single photon emission computed tomography (SPECT) imaging techniques.[7−12] VEGF$_{121}$, being a natural ligand of VEGFR and possessing high binding affinity for VEGFR-2, is an excellent candidate for targeted molecular

imaging.[13] However, direct radiolabeling of targeting ligands might alter their in vivo pharmacokinetics and compromise the binding affinity. Besides, the presence of only a few conjugation sites limits the potential of conjugating other functional moieties (e.g., fluorescent dyes, anticancer drugs) to the targeting ligands. Thus, engineering of a multifunctional platform, which can harbor VEGFR targeting ligands (e.g., VEGF$_{121}$), imaging moieties (e.g., copper-64 [^{64}Cu]) as well as therapeutic agents (e.g., hydrophilic and hydrophobic anti-cancer drugs) together in one nanosystem for effective VEGFR targeted cancer imaging and therapy, is highly desired.

One of the major challenges pertaining to the suboptimal performance of many anticancer drugs is the low bioavailability and inefficient delivery to the target site.[14] A lot of anticancer drugs are hydrophobic and need biocompatible drug delivery systems to enable improved bioavailability and facilitate easier intravenous administration. Silica is considered as "Generally Recognized As Safe" (GRAS) by the U.S. Food and Drug Administration (FDA) and silica based C-dots (or Cornell
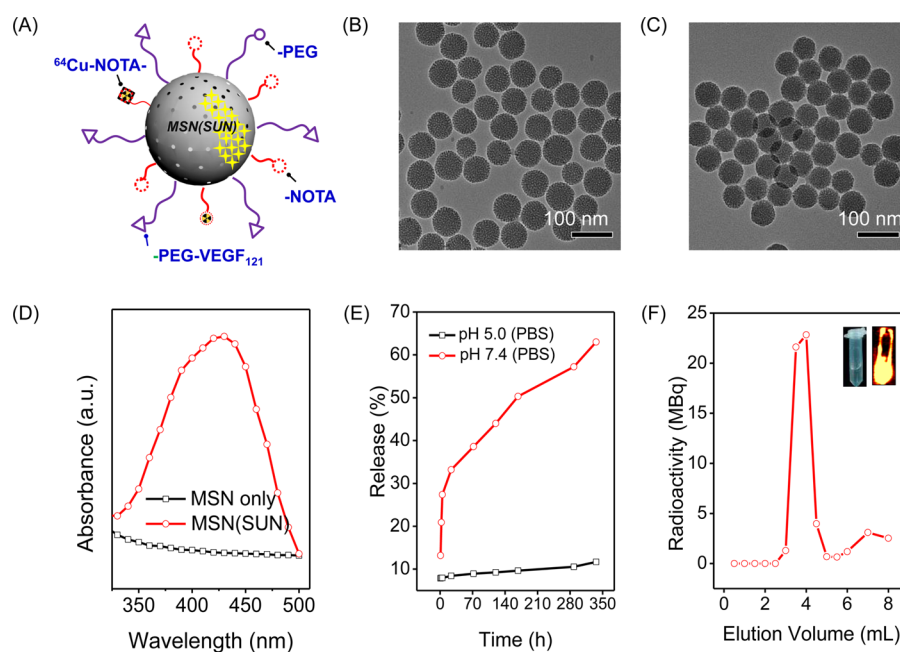
Figure 1. Synthesis and characterization of ^{64}Cu-NOTA-MSN(SUN)-VEGF[121]. (A) Schematic illustration of ^{64}Cu-NOTA-MSN(SUN)-VEGF[121] nanoconjugate. (B) Transmission electron microscopy (TEM) image of pure MSN before surface modification. (C) TEM image of NOTA-MSN(SUN)-VEGF[121]. (D) UV−vis spectrum of pure MSN (black line) and sunitinib loaded MSN, or MSN(SUN) (red line). (E) In vitro drug release profile of MSN(SUN) in PBS with different pH values. (F) Elution profile of ^{64}Cu-NOTA-MSN-VEGF[121] after the ^{64}Cu labeling. Inset shows the digital photo and PET imaging of ^{64}Cu-NOTA-MSN-VEGF[121] (3.5−4.0 mL fraction).

dots) are among the first inorganic nanoparticles to be approved for first-in-human trial by the FDA.[15,16] Mesoporous silica nanoparticles (MSNs) have recently been extensively studied as drug carriers owing to their large pore volumes, high surface area, superior biocompatibility, nontoxicity and easily modifiable surface.[17−19] MSNs, as exipients for drug formulations, can offer a promising approach to overcome the insolubility issue and deliver large payloads of hydrophobic small molecule drugs.[20,21] Besides the potential for loading large amounts of drug, the silanol bearing surface can further be easily modified for enhanced pharmacokinetics or stimuli responsive release of the drugs.[22] However, engineering of MSN for in vivo actively targeted drug delivery is still one of the major challenges in this field, and most of the previously reported silica-based drug delivery system studies were focused on passive tumor targeting, which relies on unpredictable tumor extravasation and enhanced permeability retention (EPR) effect.[14,20,23−26]

Inspired by the pivotal role of the VEGF/VEGFR signaling pathway in cancer and the advantages offered by MSNs, in this paper, we propose a VEGF pathway targeting potentially theranostic nanoplatform (Figure 1A) based on surface engineering of MSN for simultaneous noninvasive PET imaging and in vivo enhanced delivery of anti-VEGFR drug, sunitinib (SUN). Human glioblastoma (U87MG) bearing mice with suitable tumor sizes (∼60 mm³, having high VEGFR expression) were selected for in vivo active targeting study. Uniform sized MSN was first surface modified with amino groups, followed by chelator (e.g., S-2-(4-isothiocyanatobenzyl)-1,4,7-triazacyclononane-1,4,7-triacetic acid, or NOTA) conjugation, PEGylation, VEGF[121] linkage and radioisotope (^{64}Cu, $t_{1/2}$ = 12.7 h) labeling. The mesoporous scaffolds were loaded with a small molecule hydrophobic drug to assess their drug loading and delivery efficacy. Sunitinib was chosen because it is a potent receptor tyrosine kinase inhibitor

(including all VEGFRs) and has been clinically successful in providing improved progression free survival and tumor responses in a range of cancers.[27−31] To the best of our knowledge, this is the first study documenting the use of MSNs for VEGFR targeted PET imaging and in vivo enhanced drug delivery.

■ EXPERIMENTAL SECTION

Materials. K3-VEGF[121] was purchased from Corp. (Piscataway, NJ). p-SCN-Bn-NOTA was acquired from Macrocyclics, Inc. (Dallas, TX). Mal-PEG[5k]-SCM was purchased from Creative PEGworks (Winston Salem, NC). NHS-fluorescein and Chelex 100 resin (50−100 mesh), tetraethyl orthosilicate (TEOS), triethylamine (TEA), 3-aminopropylsilanetriol (APS), hexadecyl trimethylammonium chloride (CTAC, 25 wt %) and dimethyl sulfoxide (DMSO) were obtained from Sigma-Aldrich (St. Louis, MO). Cy3-labeled secondary antibody was purchased from Jackson Immunoresearch Laboratories, Inc. (West Grove, CA). Sunitinib malate was purchased from Tocris Biosciences (Minneapolis, MN). PD-10 columns were bought from GE Healthcare (Piscataway, NJ). Absolute ethanol and sodium chloride (NaCl) were obtained from Fisher Scientific. Water and all buffers were of Millipore grade and pretreated with Chelex 100 resin to ensure that the aqueous solution was free of heavy metals. All chemicals were used as received without further purification.

Characterization. Transmission electron microscopy (TEM) analysis was performed on a FEI T12 microscope. Dilute solutions of as prepared and functionalized MSNs were placed dropwise onto carbon-coated copper grids and allowed to dry. TEM images were taken at an accelerating voltage of 120 kV. DLS and zeta potential analysis were performed on Nano-Zetasizer (Malvern Instruments Ltd.).

Synthesis of Uniform 80 nm Sized MSNs. MSNs with a uniform diameter of ∼80 nm were synthesized using the soft template method as previously described in the literature.[32] In a typical synthesis, CTAC (2 g) and TEA (20 mg) were dissolved in high Q water (20 mL) and stirred at room temperature for 1 h. Then 1 mL of TEOS was added rapidly and the resulting mixture was again stirred for 1 h in a 95 °C water bath. The mixture was cooled down to room

temperature. The pellet collected by centrifugation at 10 000 rpm was washed with water and ethanol to remove the residual reactants. The final product was extracted with a 1 wt % solution of NaCl in methanol at room temperature to completely remove the CTAC template. The process was carried out at least three times (24 h each time). After the final wash, the nanoparticles were suspended in 20 mL absolute ethanol for amine modification.

Synthesis of Amine Modified MSNs (MSN-NH$_2$). Amine modification of the as synthesized MSNs was carried out to enable further surface functionalization. To 20 mL of MSNs in absolute ethanol solution, 1 mL of APS was added and the system sealed tight. The mixture was kept in 80−90 °C water bath for 48 h. This was followed by repeated centrifugation and washing with ethanol to remove any unreacted APS. MSN-NH$_2$ was then dispersed in water and concentration of amine groups was measured using ninhydrin-KCN (Kaiser) test.

Synthesis of VEGF$_{121}$-SH. K$_3$-VEGF$_{121}$ was first incubated with Trauts' Reagent (in 1:20 ratio) at pH 8.0 for 3 h to yield VEGF$_{121}$-SH. The recombinant human VEGF$_{121}$ used in this study had three lysine residues fused at the N-terminal to allow easier functionalization without affecting the VEGFR binding affinity. Free Traut's reagent was removed by purification by size exclusion chromatography on PD-10 columns, using phosphate buffered saline (PBS) as mobile phase.

Synthesis of NOTA-MSN-PEG-VEGF$_{121}$ and FITC-NOTA-MSN-PEG-VEGF$_{121}$. 1 mL of MSN-NH$_2$ (containing ∼100 nmol of -NH$_2$ groups) in water was reacted with p-SCN-Bn-NOTA (∼45 nmol, 5 μL of 5 mg/mL solution in DMSO) at pH 8.5 to obtain NOTA-MSN-NH$_2$. Unreacted p-SCN-Bn-NOTA was removed by centrifugation. To this, 5 mg (1000 nmol) of Mal-PEG$_{5k}$-SCM was added and reacted for another 1 h at pH 8.5, resulting in NOTA-MSN-PEG-Mal. Excess PEG molecules were again removed by centrifugation. To obtain NOTA-MSN-PEG-VEGF$_{121}$, NOTA-MSN-PEG-Mal was reacted with VEGF$_{121}$-SH in 1:5 ratio, in the presence of tris(2-carboxyethyl)-phosphine (TCEP) at pH 7.5, overnight.

To synthesize fluorescein conjugated MSN-PEG-VEGF$_{121}$ for flow cytometry and histology studies, ∼64 nmol of FITC in DMSO was reacted together with MSN-NH$_2$ at pH 8.5−9 followed by NOTA, PEG and VEGF$_{121}$ conjugations as described above.

Sunitinib Loading and Release in Vitro. NOTA-MSN(SUN)-PEG-VEGF$_{121}$ was obtained by mixing SUN (1 mg/mL in DMSO) with MSN-NH$_2$ (3.5 mg) on a shaker for 24 h. Excess sunitinib-DMSO solution was removed by centrifugation, followed by subsequent washing with water for three times. NOTA, PEG and VEGF$_{121}$ conjugations were carried out in further reactions, as outlined above. The final conjugate was dispersed in PBS for further in vitro and in vivo studies.

SUN absorbance (absorbance maximum at ∼430 nm) determined with UV−vis spectroscopy was used to determine the amount of SUN loaded into MSNs. Loading capacity was calculated using the following formula: (amount of SUN in MSN/amount of MSN) × 100%. The release studies were carried out in PBS (pH 7.4 and pH 5.0) for 2 weeks. SUN loaded MSNs were dispersed in 1 mL of solution of both types. At predetermined time-points, the solutions were spun down in a centrifuge and supernatants collected and analyzed on a UV−vis spectrometer. New solution was replenished after each time-point.

Cell Lines and Animal Model. U87MG human glioblastoma multiforme, human umbilical vein endothelial cells (HUVECs) and 4T1 murine breast cancer cell lines were purchased from the American Type Culture Collection (ATCC, Manassas, VA). U87MG and 4T1 cells were cultured in Dulbecco's modified Eagle's medium (DMEM) and RPMI 1640 media (Invitrogen, Carlsbad, CA) respectively, with 10% fetal bovine serum at 37 °C with 5% CO$_2$. Cells were allowed to reach 75% confluence before use. All animal studies were conducted under a protocol approved by the University of Wisconsin Institutional Animal Care and Use Committee. The U87MG tumor model was generated by subcutaneous injection of 2 × 10^6 cells in 100 μL of a phosphate buffered saline (PBS):Matrigel (BD Biosciences, Franklin Lakes, NJ) (1:1) mixture into the front flank of six-week-old female athymic nude mice (Harlan, Indianapolis, IN). Tumor sizes were monitored every alternate day. Mice were used for in vivo experiments when the diameter of tumors reached 4−6 mm (typically 3 weeks after inoculation).

In Vitro Flow Cytometry. Both HUVEC and 4T1 cells were harvested and suspended in cold PBS containing 2% bovine serum albumin at a concentration of 5 × 10^6 cells/mL and then incubated with fluorescein conjugated MSN-PEG-VEGF$_{121}$ or fluorescein conjugated MSN-PEG at a concentration of 5 nM for 30 min at room temperature. The cells were washed for three times with cold PBS and centrifuged for 5 min. A BD FACSCalibur four-color analysis cytometer, equipped with 488 and 633 nm lasers (Becton-Dickinson, San Jose, CA), was used to analyze the cells and data interpretation was carried out with FlowJo analysis software (Tree Star, Ashland, OR).

^{64}Cu Labeling and Serum Stability Studies. 148 MBq of ^{64}CuCl$_2$ was diluted in 300 μL of 0.1 M sodium acetate buffer (pH 6.5) and added to NOTA-MSN-PEG-VEGF$_{121}$ or NOTA-MSN-PEG and reacted at 37 °C for 30 min under constant shaking. ^{64}Cu labeled conjugates were then purified on PD-10 columns using Chelex-100 pretreated PBS as the mobile phase. The radioactivity fractions (typically eluting between 3.5 and 4.5 mL) were collected for further in vitro and in vivo experiments. The unreacted ^{64}Cu fraction is expected to elute from the column after 6 mL of PBS. The whole procedure of ^{64}Cu labeling and purification of the MSNs was completed in 90 ± 10 min (n = 10).

Serum stability studies of ^{64}Cu-NOTA-MSN-PEG-VEGF$_{121}$ and ^{64}Cu-NOTA-MSN-PEG were carried out by incubating the radio-conjugates in complete mouse serum at 37 °C for up to 24 h (the time period of investigation for serial PET imaging, approximately two half-lives of ^{64}Cu). The mixtures were sampled at different time-points and passed through 100 kDa cutoff filters. The filtrates were collected, and the radioactivity was measured. The retained ^{64}Cu percentages were calculated for both ^{64}Cu-NOTA-MSN-PEG-VEGF$_{121}$ and ^{64}Cu-NOTA-MSN-PEG using the following equation:

[(total radioactivity − radioactivity in filtrate)/total radioactivity] × 100%.

In Vivo PET Imaging and Biodistribution Studies. Tumor-bearing mice were each injected with 5−10 MBq of ^{64}Cu-NOTAMSN-PEG-VEGF$_{121}$ or ^{64}Cu-NOTA-MSN-PEG via tail vein before serial PET scans. PET scans on microPET/microCT Inveon rodent model scanner (Siemens Medical Solutions USA, Inc.), image reconstruction and ROI analysis of the PET data were performed using described previously procedures.[33] Quantitative PET data was presented as percentage injected dose per gram of tissue (%ID/g).

After the last time-point at 22 h postinjection (p.i.), mice were euthanized and biodistribution studies were carried out to validate the %ID/g values and radioactivity distribution based on PET imaging in tumor-bearing mice. Blood, U87MG tumor, and major organs/tissues were collected and wet-weighed. The radioactivity in the tissues was measured using a γ-counter (PerkinElmer) and presented as %ID/g (mean ± SD).

Histology. U87MG tumor-bearing mice were injected with fluorescein conjugated NOTA-MSN-PEG-VEGF$_{121}$ or fluorescein conjugated NOTA-MSN-PEG (5 mg/kg of mouse body weight) and euthanized at 3 h p.i. (the point of maximum tumor uptake based on PET imaging). Organs including U87MG tumor, liver, spleen and muscle were excised, frozen and cryosectioned for histological analysis. The slices were stained for endothelial marker CD31 by using a rat antimouse CD31 antibody and a Cy3-labeled donkey antirat IgG. All images were acquired with a Nikon Eclipse Ti microscope.

In Vivo Enhanced SUN Delivery. For drug delivery studies, SUN loaded MSN-NH$_2$ was then conjugated with NOTA, PEG and VEGF$_{121}$ as described previously to form NOTA-MSN(SUN)-PEG-VEGF$_{121}$. Nontargeted nanoconjugates (i.e., NOTA-MSN(SUN)-PEG) were used as a control. For in vivo enhanced drug delivery study, U87MG tumor bearing mice were intravenously injected with NOTA-MSN(SUN)-PEG-VEGF$_{121}$ or NOTA-MSN(SUN)-PEG (5 mg nanoconjugate/kg of mouse). The mice were then sacrificed at 3 h p.i. U87MG tumor and the major organs were harvested and imaged on IVIS Spectrum preclinical imaging system (ex = 430 nm; em = 640 nm) under similar experimental conditions.

■ RESULTS AND DISCUSSION

Synthesis and Characterization of NOTA-MSN-PEG-VEGF$_{121}$. Uniform MSNs with an average size of about 80 nm were synthesized using a well-established literature procedure.[32] The nanoparticles possessed a worm-like mesoporous network of channels, as seen under TEM (Figure 1B), with a high specific surface area of 238 m^2/g and pore size of ~2.2 nm, described in our previous paper.[34] To aid in further functionalization, as-prepared MSNs were surface modified with amino groups (Scheme 1), using APS (i.e., 3-amino-

Scheme 1. Schematic Illustration of Stepwise Surface Modification and Drug Loading of MSN^a
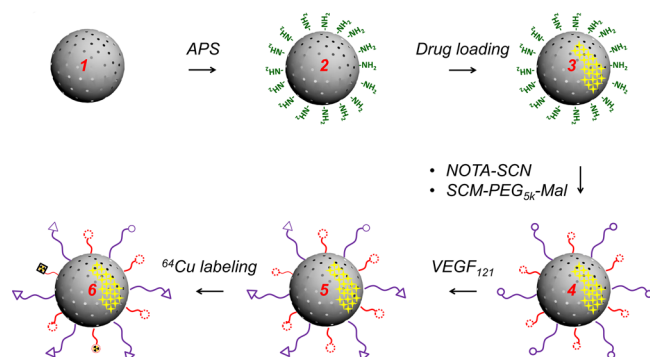
^{a}The surface of monodispersed MSN (1) was modified with amino groups (−NH$_2$) to form MSN-NH$_2$ (2). MSN-NH$_2$ was then loaded with SUN in the presence of DMSO to form MSN(SUN) (3), followed by conjugation with NOTA and subsequent PEGylation to yield NOTA-MSN(SUN)-PEG (4). Further reaction of the nanoconjugates with VEGF$_{121}$-SH yielded NOTA-MSN(SUN)-PEG-VEGF$_{121}$ (5). Finally, the nanoconjugates were radiolabeled with with ^{64}Cu to form ^{64}Cu-NOTA-MSN(SUN)-PEG-VEGF$_{121}$ (6).

propylsilanetriol) to yield MSN-NH$_2$. A hydrophobic drug (i.e., sunitinib) was then loaded into MSN by shaking the mixture of sunitinib and MSN in dimethyl sulfoxide (DMSO) for 24 h. As-obtained MSN(SUN) exhibited the characteristic absorbance spectrum of SUN (absorbance max: 430 nm), indicating the successful loading of the drug into the mesoporous channels of MSN (Figure 1D). Characteristic excitation/emission spectra of SUN in DMSO are shown in Figure S1 (Supporting Information). The loading capacity of SUN in MSNs was found to be ~100 mg of drug per g of nanoparticles. The drug release profile in PBS (pH 7.4) showed negligible release of SUN over 2 weeks, with enhanced release rate observed at lower pH values of around 5.0 (Figure 1E), possibly due to the protonation of silanol groups at lower pH, leading to the weakening of interactions between SUN and MSNs.

Afterward, desired amount of NOTA was added to obtain NOTA-MSN(SUN)-NH$_2$. The nanoparticles were then PEGylated using heterobifunctional Mal-PEG$_{5k}$-SCM; (Mal, malemide; SCM, succinidyl carboxy methyl ester), to generate NOTA-MSN-PEG-Mal. Thiolated VEGF$_{121}$ (i.e., VEGF$_{121}$-SH, see the Experimental Section) was then conjugated to obtain NOTA-MSN-PEG-VEGF$_{121}$ based on the thiol-maleimide reaction chemistry. For in vivo PET imaging, radiolabeling with ^{64}Cu was performed to yield the ^{64}Cu-NOTA-MSN-PEG-VEGF$_{121}$ nanoconjugate.

TEM analysis indicates no obvious morphology changes before and after the surface modifications, as shown in Figure 1C. The hydrodynamic diameters and surface charge of as-synthesized nanoconjugates were measured using dynamic light scattering (DLS) and ζ-potential after each step of conjugation. As expected, DLS showed larger size when compared with that measured from TEM, owing to the presence of the hydrated shell. An increase in size after subsequent surface modifications reflects the successful addition of NOTA, PEG molecules and targeting moieties on the surface of MSN at each step (Table 1). In addition, surface charge varied as expected after each step

Table 1. Variation in the DLS Diameters of the Nanoparticles after Successive Surface Modification steps

nanoparticles	DLS diameter (nm)	PDI
MSN	88.5 ± 2.2	0.040 ± 0.002
MSN-NH$_2$	102.5 ± 4.6	0.137 ± 0.007
NOTA-MSN	115.0 ± 3.6	0.137 ± 0.019
NOTA-MSN-PEG	125.2 ± 0.9	0.251 ± 0.019
NOTA-MSN-PEG-VEGF$_{121}$	129.1 ± 1.5	0.183 ± 0.021

of the conjugation; from −25.9 ± 0.5 mV (MSN only) to +47.5 ± 0.7 mV after amine modification, and then to −38.5 ± 2.3, −10.9 ± 0.7 and −10.2 ± 0.7 mV, respectively, after subsequent NOTA, SCM-PEG-Mal and VEGF$_{121}$ conjugations. The stability of NOTA-MSN-PEG$_{5k}$-VEGF$_{121}$ nanoconjugates were monitored over several weeks with no obvious aggregation observed (pH 7.4 in PBS).

Radiolabeling and Serum Stability. To radiolabel NOTA-MSN-PEG-VEGF$_{121}$ and NOTA-MSN-PEG, both nanoconjugates were reacted with ^{64}Cu for 30 min at pH 5.5, and purified on PD-10 columns using PBS as the mobile phase (to get rid of free nonchelated ^{64}Cu). Our radiolabeling elution profile showed that ^{64}Cu-NOTA-MSN-PEG-VEGF$_{121}$ eluted between 3.5 and 4.5 mL from the column, whereas free ^{64}Cu appears after 6.0 mL (Figure 1F). The radioactive fractions were then collected for further in vivo imaging. A phantom PET scan of ^{64}Cu-NOTA-MSN-PEG-VEGF$_{121}$ (inset in Figure 1F) after PD-10 purification (fraction 3.5−4.5 mL) was also conducted to prove the success of radiolabeling.

Stability of radiometals in certain tracers is a critically important aspect influencing the overall in vivo behavior and biodistribution. Research showed that free ^{64}Cu could possibly transchelate with serum proteins and result in nonselective binding or off-target accumulation, leading to erroneous interpretation of the imaging data.[35] Hence, the stability of ^{64}Cu-NOTA-MSN-PEG-VEGF$_{121}$ nanoconjugates in whole mouse serum was carefully investigated. Our results showed an excellent stability for both nanoconjugates, with over 90% ^{64}Cu radioisotopes still attached after the incubation in whole mouse serum for 24 h at 37 °C (Figure S2, Supporting Information).

In Vitro VEGFR Targeting. To assess whether VEGF$_{121}$ maintains its binding affinity and specificity for VEGFR upon conjugation with MSN, systematic flow cytometry study was carried out. Human umbilical vein endothelial cells (HUVECs) that show a high level of VEGFR expression were chosen as the VEGFR positive cell line, whereas 4T1 (a murine breast cancer cell) was selected as the VEGFR negative cell line.

MSN-NH$_2$ was first reacted with NHS-fluorescein (ex = 494 nm; em = 518 nm, NHS: N-hydroxy-succinimidyl), followed by NOTA conjugation, PEGylation and VEGF$_{121}$ conjugation to form fluorescein conjugated NOTA-MSN-PEG-VEGF$_{121}$. Nontargeted nanoparticles (i.e., fluorescein conjugated NOTA-MSN-PEG) were prepared using the same way but without the

VEGF$_{121}$ targeting moiety. As shown in Figure 2A, strong fluorescence signals were observed from HUVECs when
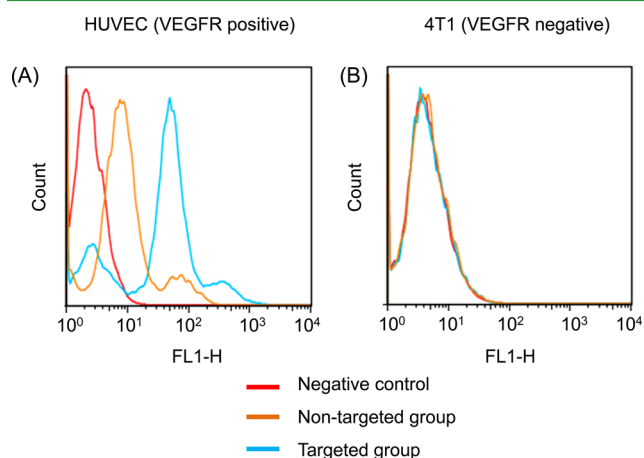
Figure 2. In vitro VEGFR targeting. Flow cytometry analysis of fluorescein conjugated MSN nanoconjugates in (A) HUVECs (VEGFR positive cell line), and (B) 4T1 murine breast cancer cell (VEGFR negative cell line).

incubated with fluorescein conjugated MSN-PEG-VEGF$_{121}$ (targeted group, 5 nM), whereas only background fluorescence was observed on incubation with fluorescein conjugated MSN-PEG (non-targeted group, 5 nM). About a 50-fold enhancement in fluorescence intensity was observed in the targeted group when compared with unstained cells (negative control). In contrast, low nonspecific binding was observed from VEGFR negative 4T1 breast cancer cells, as evidenced by background levels of fluorescence signal in all the groups (Figure 2B). All the results encouraged further in vivo investigation of VEGFR targeting efficacy. The binding of VEGF$_{121}$ tagged MSN was further found to be highly specific and did not vary appreciably with the change of particle concentrations (Figure S3, Supporting Information). A similar enhancement in fluorescence intensities (~50-fold) was observed when incubating with 25 nM and 100 nM fluorescein conjugated MSN-PEG-VEGF$_{121}$. The binding of fluorescein conjugated MSN-PEG remained still low with increased concentration, indicating low nonspecific binding of our nanoconjugates in vitro (Figure S3, Supporting Information). To further confirm that the enhanced fluorescence was indeed due to specific binding of to VEGFR, in vitro blocking study was also performed. An excess amount (~0.05 mg) of VEGF$_{121}$ was added to HUVECs prior to the addition of fluorescein conjugated MSN-PEG-VEGF$_{121}$. Significantly low fluorescence enhancement (~1.4 fold) was observed (Figure S3, Supporting Information), even with the addition of 100 nM of the targeted nanoconjugates, clearly indicating the specific VEGFR targeting of our nanoconjugates.

In Vivo VEGFR Targeted PET Imaging. Malignant glioblastomas are among the most angiogenic cancers, with VEGF being the dominant angiogenic mediator.[36] To determine the VEGFR targeting efficacy and in vivo biodistribution patterns of as-synthesized nanoconjugates, serial whole body PET scans were carried out at multiple time-points (0.6, 3, 6 and 22 h postinjection [p.i.]). For this purpose, about 7.4−11.1 MBq of ^{64}Cu-NOTA-MSN-PEG-VEGF$_{121}$ and ^{64}Cu-NOTA-MSN-PEG were intravenously injected (i.v.) in U87MG glioblastoma xenografted mice (n = 3). Figure 3 shows the tumor (marked with an arrow) containing slices of
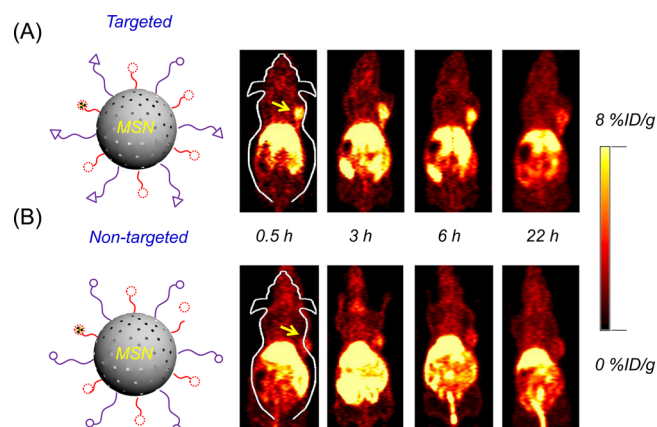

Figure 3. In vivo VEGFR targeted PET imaging in U87MG tumor bearing mice. Coronal PET images of (A) ^{64}Cu-NOTA-MSN-PEG-VEGF$_{121}$ and (B) ^{64}Cu-NOTA-MSN-PEG injected intravenously in U87MG tumor bearing mice at different time-points. The yellow arrows indicate the location of the tumor.

the coronal PET images at various time-points. The data obtained from the region-of-interest (ROI) quantification of the PET images is also presented in Figure 4A,B.

As apparent from the PET images, the uptake of ^{64}Cu-NOTA-MSN-PEG-VEGF$_{121}$ and ^{64}Cu-NOTA-MSN-PEG in the liver was prominent at early time-points and declines gradually. Such a behavior is expected for intravenously injected nanomaterials and can be attributed to the hepatic clearance of the intravenously injected nanoparticles by liver, which functions as the major organ in the reticulo-endothelial system (RES). Liver uptake of ^{64}Cu-NOTA-MSN-PEG-VEGF$_{121}$ and ^{64}Cu-NOTA-MSN-PEG was 24.2 ± 1.3 and 23.9 ± 3.5 percentage injected dose per gram (%ID/g) of tissue, respectively, at 0.5 h p.i., decreasing gradually to 11.2 ± 0.8 and 13.5 ± 1.7%ID/g, respectively, at 22 h p.i. (n = 3).

Successful in vivo VEGFR targeting was substantiated by the rapid and specific accumulation of ^{64}Cu-NOTA-MSN-PEG-VEGF$_{121}$ (6.8 ± 0.2%ID/g) in U87MG tumor as early as 0.5 h p.i., reaching a maximum of 7.8 ± 0.2%ID/g at 3 h p.i. Nontargeted ^{64}Cu-NOTA-MSN-PEG nanoconjugates, on the other hand, showed much lower tumor uptake, peaking to 2.6 ± 0.6%ID/g at 3 h p.i., indicating minimum passive targeting efficacy of the nanoparticle in U87MG tumor. It is of note that the uptake of the nanoconjugates in organs such as liver, spleen and muscle remained similar in both the targeted and non-targeted groups, while the tumor uptake remained significantly different at all time-points (Figure 4A,B). These results clearly indicate that the in vivo pharmacokinetics and biodistribution of the targeted and non-targeted nanoparticles are comparable; and thus, VEGFR specific binding was the main factor responsible for enhanced tumor uptake of ^{64}Cu-NOTA-MSN-PEG-VEGF$_{121}$ over ^{64}Cu-NOTA-MSN-PEG. The stark contrast in the tumor uptake and tumor-to-muscle ratios between the targeted and non-targeted groups at different time points is also shown in Figure 4C and Table S3 (Supporting Information), respectively.

Only two systematic in vivo active targeting studies with MSNs have been reported in the literature.[34,37] Moreover, to the best of our knowledge, despite being an attractive target, nanoparticle mediated VEGFR targeting has only been reported once earlier, where VEGF$_{121}$ conjugated quantum dots (QDs) were used for dual PET and NIRF (i.e., near-
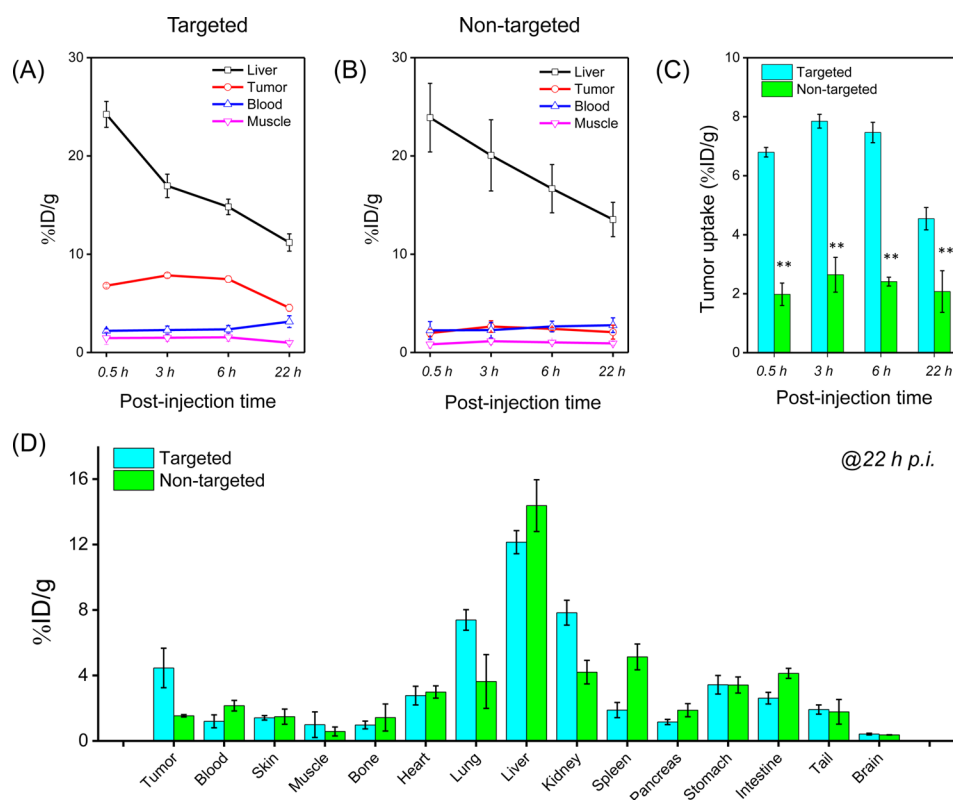
Figure 4. ROI quantification and biodistribution studies. Time-activity curves of the liver, U87MG tumor, blood, and muscle upon i.v. injection of (a) ^{64}Cu-NOTA-MSN-PEG-VEGF$_{121}$ (targeted group), and (b) ^{64}Cu-NOTA-MSN-PEG (non-targeted group). (c) U87MG tumor uptake comparison between targeted and non-targeted groups. The difference between U87MG tumor uptake in targeted group and non-targeted group was statistically significant (**$P < 0.01$). (d) Ex vivo biodistribution study of two groups at 22 h p.i. ($n = 3$ for all groups).

infrared fluorescence) imaging.[38] It is noteworthy that the highest U87MG uptake of QD-VEGF$_{121}$ reached about 4.2 ± 0.5% ID/g at 22 h p.i. While VEGF$_{121}$ conjugated MSN showed a much higher and faster accumulation in the same tumor model in the current study. Moreover, the off-target uptake of our nanoconjugates was much lower (about 24%ID/g) compared to the previous study, which was reported to be about 50%ID/g uptake in liver.[38] These results further validate the superiority of mesoporous silica nanostructures as potential vehicles for tumor vasculature targeted imaging.

Ex Vivo Biodistribution Studies. Ex vivo organ distribution studies were performed in all mice after terminal PET scans at 22 h p.i. (Figure 4D). The biodistribution values corroborated well with ROI quantification values from PET images (taken at 22 h p.i.) for both targeted and non-targeted cohorts. As expected, the major clearance organs, i.e. liver, kidney and intestine, showed enhanced accumulation of ^{64}Cu-NOTA-MSN-PEG-VEGF$_{121}$ (12.1 ± 0.7, 7.8 ± 0.7 and 2.6 ± 0.4%ID/g, respectively), indicating that the nanoparticles cleared through both hepatobiliary and renal routes. Tumor uptake was still prominent at 4.5 ± 1.2%ID/g. Moreover, apart from the tumor, the %ID/g values in all the major organs remained similar for the non-targeted group, further confirming the VEGFR specific tumor uptake of our nanoconjugates. The good agreement between PET and biodistribution quantification data supports the validity of noninvasive serial PET scans and ROI analyses in reflecting the real in vivo fate of surface modified MSNs.

Histological Analysis. To fully understand the biodistribution pattern in vivo and confirm PET imaging results,

immunofluorescence staining studies were performed. For this purpose, fluorescein labeled NOTA-MSN-PEG-VEGF$_{121}$ and NOTA-MSN-PEG nanoparticles were administered intravenously in much higher doses (~15 mg nanoconjugates/kg of mouse body weight) in U87MG tumor bearing mice. U87MG tumor, liver, spleen and muscle were excised, frozen and cryosectioned after euthanization of the mice ($n = 3$) at 3 h p.i.

Frozen tissue slices (6 μm thick) were stained for vascular endothelial marker CD31, using rat antimouse CD31 primary antibody and Cy3 labeled donkey antirat secondary antibody using a previously reported protocol.[39] The stained slices were observed using a Nikon Eclipse Ti microscope. The green fluorescence from fluorescein in Figure 5 indicates the location of the nanoparticles and the red fluorescence marks the position of the vessels. Excellent overlay of the red and green signals in the U87MG tumor of the targeted group indicates the vasculature specific uptake of MSN-PEG-VEGF$_{121}$ with little extravasation. Consistent with PET imaging and biodistribution studies, significant green signals were observed in both the liver and spleen tissue slices, indicating high nanoparticle uptake in these organs. However, very weak overlap was observed between the red and green fluorescence signals, indicating the nonspecific nature of the nanoparticle accumulation in these organs, due to the macrophage capture or other mechanisms. As expected, no significant green fluorescence was observed in muscle tissue, which correlated well with the PET findings. Overall, our ex vivo histological analysis of the tissues further confirms the VEGFR specific uptake of our nanoconjugates.
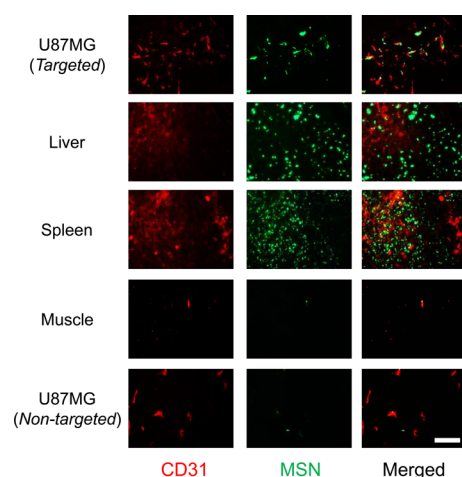
Figure 5. Ex vivo histology analysis. Immunofluorescence staining of the tissue slices with CD31 (red, with antimouse CD31 primary antibody; left panel). Fluorescein conjugated MSN nanoconjugates (green, middle panel). Merged images are also shown at the right panel. Scale bar: 100 μm.

In Vivo Enhanced Drug Delivery. Efficacy of a drug depends largely on its efficient delivery to the disease site, specifically and in large amounts. The use of MSNs as an ideal platform to carry drugs, especially hydrophobic and aromatic compounds, has been envisaged for over a decade.[20,22,25,26] However, few examples of in vivo tumor targeted drug delivery have been reported.[34] Given the importance of VEGF/VEGFR cascade in tumor angiogenesis and metastasis, a number of anti-VEGF/VEGFR therapies have been used to effectively curb cancer. However, nonspecific systemic delivery of a drug can lead to several side effects, sometimes even mortality.

We hypothesized that loading an anti-VEGFR drug into NOTA-MSN-PEG-VEGF$_{121}$ nanocarriers can be an effective strategy to improve the treatment efficacy of the drug and reduce toxicity to the nontarget organs. Therefore, as a proof-of-concept, SUN, a hydrophobic, anti-VEGFR small molecule drug, was selected for demonstrating the capability for in vivo enhanced drug delivery.

To achieve targeted SUN delivery in vivo, MSN(SUN) was stepwise conjugated to NOTA, PEG and VEGF$_{121}$, as described earlier, to produce NOTA-MSN(SUN)-PEG-VEGF$_{121}$ nanoconjugates (Figure 6A). A separate batch of NOTA-MSN-(SUN)-PEG was also synthesized to serve as a non-targeted control. Equal concentration solutions of NOTA-MSN(SUN)-PEG-VEGF$_{121}$ and NOTA-MSN(SUN)-PEG (∼500 μg/mL) were used for in vivo image-guided drug delivery studies. The final dose of SUN was about 5 mg of SUN per kg of mouse. The U87MG bearing mice were sacrificed at 3 h p.i. Fluorescence from the drug was harnessed to image the tumor along with the major organs, using an IVIS Spectrum imaging system (ex = 430 nm; em = 640 nm). An equal concentration of MSNs without SUN was also injected in a separate group of mice to serve as the negative control. Enhanced delivery of SUN to U87MG tumors was achieved in targeted group when compared with the non-targeted group (Figure 6C). Moreover, the negative control group showed only background levels of fluorescence in all organs, lower than even the non-targeted group, indicating that autofluorescence from the organs was not responsible for the observed effects. The accumulation in RES organs, such as liver and spleen,
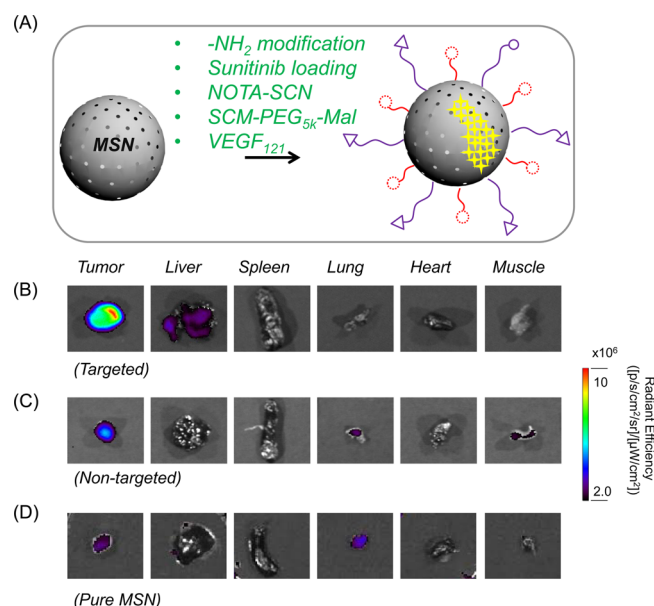
Figure 6. In vivo enhanced drug delivery study. (A) Schematic illustration showing the synthesis of NOTA-MSN(SUN)-PEG-VEGF$_{121}$ for in vivo enhanced drug delivery. Ex vivo optical images of sunitinib in major organs at 3 h p.i. of (B) NOTA-MSN(SUN)-PEG-VEGF$_{121}$ (targeted group), (C) NOTA-MSN(SUN)-PEG (non-targeted group) in U87MG bearing mice, and (D) pure MSN without the drug SUN (negative control). All images were acquired using an IVIS spectrum in vivo imaging system (ex = 430 nm; em = 640 nm).

appeared low, contrary to the PET imaging results. This anomaly can be explained on the basis of different absorption and scattering of SUN emission (around 580 nm) signal by different tissues. Therefore, dark colored organs, such as liver and spleen, may have strongly absorbed the emission wavelength from SUN, resulting in a weaker optical signal, compared to the light colored tumor tissues. As such, optical imaging cannot reliably measure the accurate absolute uptake of MSN(SUN) in different organs. However, it can serve as a handy tool to compare the drug uptake in U87MG tumors from the targeted and non-targeted groups. About a 2-fold difference was observed between the two groups, clearly demonstrating the superiority of using VEGF$_{121}$ targeted MSNs for enhanced delivery of anti-VEGFR drugs over passively targeted nanosystems.

■ CONCLUSION

In conclusion, VEGFR targeting with nanoparticles is a vastly unexplored area in the literature and can serve to home imaging agents and therapeutics simultaneously and specifically to tumor vasculature. In this study, we report the design, synthesis and characterization of VEGFR targeted mesoporous silica nanostructures. Extensive in vitro, in vivo and ex vivo studies confirmed the stability and VEGFR specific targeting ability of ^{64}Cu-NOTA-MSN-PEG-VEGF$_{121}$ nanoconjugates. In vivo PET imaging studies indicated an almost 3-fold enhancement in the tumor accumulation of targeted MSNs when compared to the non-targeted group, while the uptake in the other organs remained similar. The excellent target specificity of our nanoconjugates was also harnessed for preliminary site specific delivery of an anti-VEGFR drug (i.e., sunitinib) to U87MG tumors. Overall, the encouraging results obtained in our study indicate that VEGFR targeting with VEGF$_{121}$ conjugated, anti-

VEGFR therapeutics loaded MSN may represent a major advance for angiogenesis imaging and inhibition in lethal cancers.

■ ASSOCIATED CONTENT

ⓢ Supporting Information

Tables S1−S2 list the uptake of nanoconjugates in targeted and non-targeted cohorts at different time-points. Table S3 indicates the tumor to muscle ratios of accumulation of targeted and non-targeted nanoconjugates. Figures S1 and S2 indicate the excitation/emission spectra of sunitinib drug and fidelity of ^{64}Cu to the nanoconjugates, respectively. Figure S3 depicts flow cytometry data at various concentrations of the nanoconjugates. Figure S4 compares the fluorescence signals of sunitinib loaded targeted and non-targeted nanoparticle solutions with the negative control (nanoparticle only). This material is available free of charge via the Internet at http://pubs.acs.org.

■ AUTHOR INFORMATION

Corresponding Author

*Prof. Weibo Cai. E-mail: wcai@uwhealth.org.

Present Address

^{1}Departments of Radiology and Medical Physics, University of Wisconsin−Madison, Room 7137, 1111 Highland Avenue, Madison, WI 53705-2275, United States

Author Contributions

⊗The paper was written by S. Goel, F. Chen and W. Cai. All authors have given approval to the final version of the paper. S. Goel and F. Chen contributed equally to this work.

Notes

The authors declare no competing financial interest.

■ ACKNOWLEDGMENTS

■ REFERENCES

(1) Hanahan, D.; Weinberg, R. A. Hallmarks of Cancer: The Next Generation. *Cell* **2011**, *144*, 646−674.

(2) Cai, W.; Chen, X. Multimodality Molecular Imaging of Tumor Angiogenesis. *J. Nucl. Med.* **2008**, *49* (Suppl 2), 113S−128S.

(3) Bergers, G.; Benjamin, L. E. Tumorigenesis and the Angiogenic Switch. *Nat. Rev. Cancer* **2003**, *3*, 401−410.

(4) Cristofanilli, M.; Charnsangavej, C.; Hortobagyi, G. N. Angiogenesis Modulation in Cancer Research: Novel Clinical Approaches. *Nat. Rev. Drug Discov* **2002**, *1*, 415−426.

(5) Hicklin, D. J.; Ellis, L. M. Role of the Vascular Endothelial Growth Factor Pathway in Tumor Growth and Angiogenesis. *J. Clin. Oncol.* **2005**, *23*, 1011−1027.

(6) Ellis, L. M.; Hicklin, D. J. VEGF-Targeted Therapy: Mechanisms of Anti-Tumour Activity. *Nat. Rev. Cancer* **2008**, *8*, 579−591.

(7) Chan, C.; Sandhu, J.; Guha, A.; Scollard, D. A.; Wang, J.; Chen, P.; Bai, K.; Lee, L.; Reilly, R. M. A Human Transferrin-Vascular Endothelial Growth Factor (HNTF-VEGF) Fusion Protein Containing an Integrated Binding Site for (111) in for Imaging Tumor Angiogenesis. *J. Nucl. Med.* **2005**, *46*, 1745−1752.

(8) Hsu, A. R.; Cai, W.; Veeravagu, A.; Mohamedali, K. A.; Chen, K.; Kim, S.; Vogel, H.; Hou, L. C.; Tse, V.; Rosenblum, M. G.; Chen, X. Multimodality Molecular Imaging of Glioblastoma Growth Inhibition with Vasculature-Targeting Fusion Toxin VEGF121/RGEL. *J. Nucl. Med.* **2007**, *48*, 445−454.

(9) Cai, W.; Chen, K.; Mohamedali, K. A.; Cao, Q.; Gambhir, S. S.; Rosenblum, M. G.; Chen, X. PET of Vascular Endothelial Growth Factor Receptor Expression. *J. Nucl. Med.* **2006**, *47*, 2048−2056.

(10) Zhang, Y.; Hong, H.; Niu, G.; Valdovinos, H. F.; Orbay, H.; Nayak, T. R.; Chen, X.; Barnhart, T. E.; Cai, W. Positron Emission Tomography Imaging of Vascular Endothelial Growth Factor Receptor Expression with (61)Cu-Labeled Lysine-Tagged VEGF(121). *Mol. Pharmaceutics* **2012**, *9*, 3586−3594.

(11) Zhang, Y.; Hong, H.; Engle, J. W.; Yang, Y.; Barnhart, T. E.; Cai, W. Positron Emission Tomography and near-Infrared Fluorescence Imaging of Vascular Endothelial Growth Factor with Dual-Labeled Bevacizumab. *Am. J. Nucl. Med. Mol. Imaging* **2012**, *2*, 1−13.

(12) Hao, G.; Hajibeigi, A.; Leon-Rodriguez, L. M.; Oz, O. K.; Sun, X. Peptoid-based PET Imaging of Vascular Endothelial Growth Factor Receptor (VEGFR) Expression. *Am. J. Nucl. Med. Mol. Imaging* **2011**, *1*, 65−75.

(13) Wang, H.; Chen, K.; Niu, G.; Chen, X. Site-Specifically Biotinylated VEGF(121) for near-Infrared Fluorescence Imaging of Tumor Angiogenesis. *Mol. Pharmaceutics* **2009**, *6*, 285−294.

(14) Ferris, D. P.; Lu, J.; Gothard, C.; Yanes, R.; Thomas, C. R.; Olsen, J. C.; Stoddart, J. F.; Tamanoi, F.; Zink, J. I. Synthesis of Biomolecule-Modified Mesoporous Silica Nanoparticles for Targeted Hydrophobic Drug Delivery to Cancer Cells. *Small* **2011**, *7*, 1816−1826.

(15) Rosenholm, J. M.; Mamaeva, V.; Sahlgren, C.; Linden, M. Nanoparticles in Targeted Cancer Therapy: Mesoporous Silica Nanoparticles Entering Preclinical Development Stage. *Nanomedicine (London, U. K.)* **2012**, *7*, 111−120.

(16) Benezra, M.; Penate-Medina, O.; Zanzonico, P. B.; Schaer, D.; Ow, H.; Burns, A.; DeStanchina, E.; Longo, V.; Herz, E.; Iyer, S.; Wolchok, J.; Larson, S. M.; Wiesner, U.; Bradbury, M. S. Multimodal Silica Nanoparticles Are Effective Cancer-Targeted Probes in a Model of Human Melanoma. *J. Clin. Invest.* **2011**, *121*, 2768−2780.

(17) Mamaeva, V.; Sahlgren, C.; Linden, M. Mesoporous Silica Nanoparticles in Medicine—Recent Advances. *Adv. Drug Delivery Rev.* **2013**, *65*, 689−702.

(18) Tang, F.; Li, L.; Chen, D. Mesoporous Silica Nanoparticles: Synthesis, Biocompatibility and Drug Delivery. *Adv. Mater.* **2012**, *24*, 1504−1534.

(19) Chen, Y.; Chen, H.; Shi, J. In Vivo Bio-Safety Evaluations and Diagnostic/Therapeutic Applications of Chemically Designed Mesoporous Silica Nanoparticles. *Adv. Mater.* **2013**, *25*, 3144−3176.

(20) Lu, J.; Liong, M.; Zink, J. I.; Tamanoi, F. Mesoporous Silica Nanoparticles as a Delivery System for Hydrophobic Anticancer Drugs. *Small* **2007**, *3*, 1341−1346.

(21) Li, Z.; Dong, K.; Huang, S.; Ju, E.; Liu, Z.; Yin, M.; Ren, J.; Qu, X. A Smart Nanoassembly for Multistage Targeted Drug Delivery and Magnetic Resonance Imaging. *Adv. Funct. Mater.* **2014**, *24*, 3612−3620.

(22) Yuan, L.; Tang, Q.; Yang, D.; Zhang, J. Z.; Zhang, F.; Hu, J. Preparation of pH-Responsive Mesoporous Silica Nanoparticles and Their Application in Controlled Drug Delivery. *J. Phys. Chem. C* **2011**, *115*, 9926−9932.

(23) Fan, J.; Fang, G.; Wang, X.; Zeng, F.; Xiang, Y.; Wu, S. Targeted Anticancer Prodrug with Mesoporous Silica Nanoparticles as Vehicles. *Nanotechnology* **2011**, *22*, 455102.

(24) Kim, J.; Kim, H. S.; Lee, N.; Kim, T.; Kim, H.; Yu, T.; Song, I. C.; Moon, W. K.; Hyeon, T. Multifunctional Uniform Nanoparticles Composed of a Magnetite Nanocrystal Core and a Mesoporous Silica Shell for Magnetic Resonance and Fluorescence Imaging and for Drug Delivery. *Angew. Chem., Int. Ed.* **2008**, *47*, 8438−8441.

(25) Yang, P.; Gai, S.; Lin, J. Functionalized Mesoporous Silica Materials for Controlled Drug Delivery. *Chem. Soc. Rev.* **2012**, *41*, 3679−3698.

(26) Liu, Q.; Zhang, J.; Sun, W.; Xie, Q. R.; Xia, W.; Gu, H. Delivering Hydrophilic and Hydrophobic Chemotherapeutics Simulta-

neously by Magnetic Mesoporous Silica Nanoparticles to Inhibit Cancer Cells. *Int. J. Nanomed.* **2012**, *7*, 999−1013.

(27) Kodera, Y.; Katanasaka, Y.; Kitamura, Y.; Tsuda, H.; Nishio, K.; Tamura, T.; Koizumi, F. Sunitinib Inhibits Lymphatic Endothelial Cell Functions and Lymph Node Metastasis in a Breast Cancer Model through Inhibition of Vascular Endothelial Growth Factor Receptor 3. *Breast Cancer Res.* **2011**, *13*, R66.

(28) Wood, L. Sunitinib Malate for the Treatment of Renal Cell Carcinoma. *Expert Opin. Pharmacother.* **2012**, *13*, 1323−1336.

(29) Abouantoun, T. J.; Castellino, R. C.; MacDonald, T. J. Sunitinib Induces PTEN Expression and Inhibits PDGFR Signaling and Migration of Medulloblastoma Cells. *J. Neuro-Oncol.* **2011**, *101*, 215−226.

(30) Nagengast, W. B.; Lub-de Hooge, M. N.; Oosting, S. F.; den Dunnen, W. F.; Warnders, F. J.; Brouwers, A. H.; de Jong, J. R.; Price, P. M.; Hollema, H.; Hospers, G. A.; Elsinga, P. H.; Hesselink, J. W.; Gietema, J. A.; de Vries, E. G. VEGF-PET Imaging Is a Noninvasive Biomarker Showing Differential Changes in the Tumor During Sunitinib Treatment. *Cancer Res.* **2011**, *71*, 143−153.

(31) Kreisl, T. N.; Smith, P.; Sul, J.; Salgado, C.; Iwamoto, F. M.; Shih, J. H.; Fine, H. A. Continuous Daily Sunitinib for Recurrent Glioblastoma. *J. Neuro-Oncol.* **2013**, *111*, 41−48.

(32) Pan, L.; He, Q.; Liu, J.; Chen, Y.; Ma, M.; Zhang, L.; Shi, J. Nuclear-Targeted Drug Delivery of TAT Peptide-Conjugated Monodisperse Mesoporous Silica Nanoparticles. *J. Am. Chem. Soc.* **2012**, *134*, 5722−5725.

(33) Hong, H.; Yang, K.; Zhang, Y.; Engle, J. W.; Feng, L.; Yang, Y.; Nayak, T. R.; Goel, S.; Bean, J.; Theuer, C. P.; Barnhart, T. E.; Liu, Z.; Cai, W. In Vivo Targeting and Imaging of Tumor Vasculature with Radiolabeled, Antibody-Conjugated Nanographene. *ACS Nano* **2012**, *6*, 2361−2370.

(34) Chen, F.; Hong, H.; Zhang, Y.; Valdovinos, H. F.; Shi, S.; Kwon, G. S.; Theuer, C. P.; Barnhart, T. E.; Cai, W. In Vivo Tumor Targeting and Image-Guided Drug Delivery with Antibody-Conjugated, Radio-labeled Mesoporous Silica Nanoparticles. *ACS Nano* **2013**, *7*, 9027−9039.

(35) Bass, L. A.; Wang, M.; Welch, M. J.; Anderson, C. J. In Vivo Transchelation of Copper-64 from TETA-Octreotide to Superoxide Dismutase in Rat Liver. *Bioconjugate Chem.* **2000**, *11*, 527−532.

(36) Reardon, D. A.; Wen, P. Y.; Desjardins, A.; Batchelor, T. T.; Vredenburgh, J. J. Glioblastoma Multiforme: An Emerging Paradigm of Anti-VEGF Therapy. *Expert Opin. Biol. Ther.* **2008**, *8*, 541−553.

(37) Chen, F.; Nayak, T. R.; Goel, S.; Valdovinos, H. F.; Hong, H.; Theuer, C. P.; Barnhart, T. E.; Cai, W. In Vivo Tumor Vasculature Targeted PET/NIRF Imaging with TRC105(Fab)-Conjugated, Dual-Labeled Mesoporous Silica Nanoparticles. *Mol. Pharm.* **2014**, *11*, 4007−4014.

(38) Chen, K.; Li, Z. B.; Wang, H.; Cai, W.; Chen, X. Dual-Modality Optical and Positron Emission Tomography Imaging of Vascular Endothelial Growth Factor Receptor on Tumor Vasculature Using Quantum Dots. *Eur. J. Nucl. Med. Mol. Imaging* **2008**, *35*, 2235−2244.

(39) Hong, H.; Yang, Y.; Zhang, Y.; Engle, J. W.; Barnhart, T. E.; Nickles, R. J.; Leigh, B. R.; Cai, W. Positron Emission Tomography Imaging of CD105 Expression During Tumor Angiogenesis. *Eur. J. Nucl. Med. Mol. Imaging* **2011**, *38*, 1335−1343.